ROYAL AERONAUTICAL SOCIETY

REGULAR PAPER

Simulation of pyroshock environment and effect rules of shock response spectrum

W. Wang[1,2] , K. Huang[1] and F. Zhao[3,*]

[1]School of Mechanical Engineering, University of Science and Technology Beijing, Beijing, China, [2]The Key Laboratory of Fluid and Matter Interaction, University of Science and Technology Beijing, Beijing, China and [3]National Center for Materials Service Safety, University of Science and Technology Beijing, Beijing, China
*Corresponding author. Email: zhaofei@ustb.edu.cn

Abstract

The high-frequency and high-amplitude pyroshock environment during the service of the spacecraft will cause damage to the equipment. Here, we develop a shock test device based on air cannon to simulate the above pyroshock environment. Then, a finite element model was established by explicit dynamic software ANSYS/LS-DYNA, and the simulation results were proved to be consistent with the test data. Based on the theory of Shock Response Spectrum (SRS), the effects of device parameters such as pressure, bullet material and resonant plate material on SRS were investigated via numerical simulation and shock test. This study shows that the amplitude of SRS increases with the increase of pressure in the range of 0.15–0.60 MPa, and the break frequency amplitude has a square root function relationship with the pressure. Additionally, the high-frequency amplitude of SRS was affected by the energy transfer efficiency of the bullet.

Nomenclature

Abbreviations

SDOF	Single Degree of Freedom
SRS	Shock Response Spectrum

Symbols

c	Damping of system
f_n	Natural frequency
G	Amplitude of break frequency of SRS
k	Stiffness of system
m	Mass of system
m_d	Mass of bullet
p	Pressure
v	Velocity of bullet
V	Volume of barrel
α	Correction coefficient of air cannon
$y(t)$	System response
$x(t)$	External input excitation
ω_n	Natural circular frequency
ω_d	Damped natural circular frequency
ξ	Damping coefficient

1.0 Introduction

In aerospace engineering, the pyroshock environment is one of the harshest mechanical assessment environments on spacecraft [1–3], which is extremely destructive to precision instruments and seriously threatens spacecraft safety [4–8]. Precision instruments need to undergo impact tests to assess their impact resistance before service. However, due to the characteristics of high-frequency, transient and high-amplitude of the pyroshock environment, it would be difficult to simulate accurately in the impact test [9]. Therefore, it is of great significance to further study the simulation technology of pyroshock environment.

At present, the pyroshock environment simulation devices mainly involve pyrotechnic simulation, mechanical impact simulation, vibration table simulation and laser excitation simulation. Ma [10] used explosive loading technology to conduct impact test research on instrument brackets, solenoid valves and the rocket cabin. Zhao used the explicit finite element program ANSYS/LS-DYNA to perform numerical simulation on the double-plate pyroshock environment simulation platform [11]. Pyrotechnic simulation is one of the most practical methods now, but it has obvious disadvantages of poor repeatability, high test cost and high risk. Shaking table simulation has the advantages of excellent controllability, repeatability and low cost, but it is difficult to complete the high value test of the limitation of its own technical indicators. Velmurugan studied the pyrotechnic environment simulation technology of composite resonator plates under the impact load of a light gas gun through experiment and numerical simulation [12]. Zhao found that the change in the fixing method of the resonant plate can adjust the pyroshock environment within a certain range [13]. Jang applied laser excitation technology to simulate the pyroshock environment [14, 15]. Qin studied the effects of the laser excitation method, excitation characteristics and parameters [16, 17]. However, owing to the energy limitation of the laser simulation device, the pyroshock environment is far away from reality.

Although some progress has been made in the simulation research of pyroshock environments, there are still limitations to the methods mentioned above. The mechanical impact method possesses the advantages of high repeatability and well consistency, however, such methods lack the study of the effects of SRS. Therefore, we developed a shock test device based on air cannon to simulate the pyroshock environment. A high-precision numerical simulation model is established with the aid of simulation software ANSYS/LS-DYNA. Based on the theory of SRS, the effects of the device parameters on the pyroshock environment are systematically studied. Finally, the correctness of the summary law was verified through tests. The research provides a reliable method for simulating the pyroshock environment in aerospace engineering.

2.0 Simulator of pyroshock environment

2.1 Design of simulator

The explosion shock appears as a shock wave effect in the near field, and appears as a resonance of the structure as transmitted to the far field region [18]. Since most of the spacecraft precision equipment is installed in the far-field region, the characteristics of the far field region are more concerning. The impact of the bullet loaded by the air cannon can excite the resonance response of the resonant plate, which is similar to the far-field response characteristics of the pyroshock environment.

As shown in Fig. 1, the air cannon device is composed of DN65 pneumatic globe valve, gas chamber, gun barrel and movable liftable device. The barrel diameter of the air cannon is 0.08 m, and the barrel length is 1 m. Tescom automatic pressure regulator (1.5 ± 0.01 MPa) is used to realise automatic pressure regulation, and the pressure of the air chamber is measured by the pressure transmitter (0.1% FS) to ensure that the measurement has control accuracy.

As demonstrated in Fig. 2, the resonant plate simulation device is composed of a bullet, resonant plate and test piece. Table 1 lists the parameters of each component. The shock environment is achieved by the strong collision between the rapidly ejected bullet and the resonant plate under the action of

Table 1. *Part parameters*

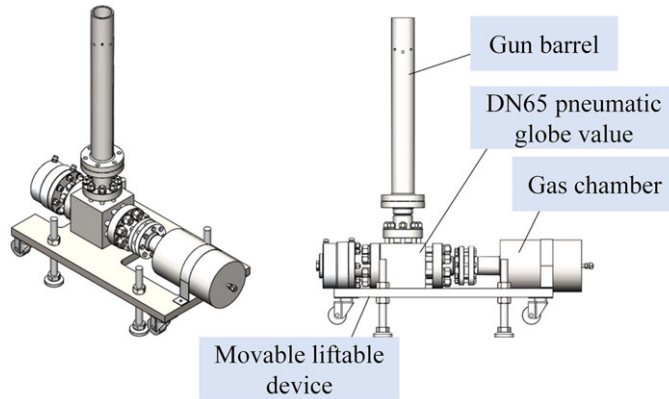| Part name	Resonant plate	Test device	Bullet
Size (mm)	$1{,}200 \times 1{,}200 \times 10$	$250 \times 250 \times 6$	Length130
Material	Steel	Steel	Aluminum

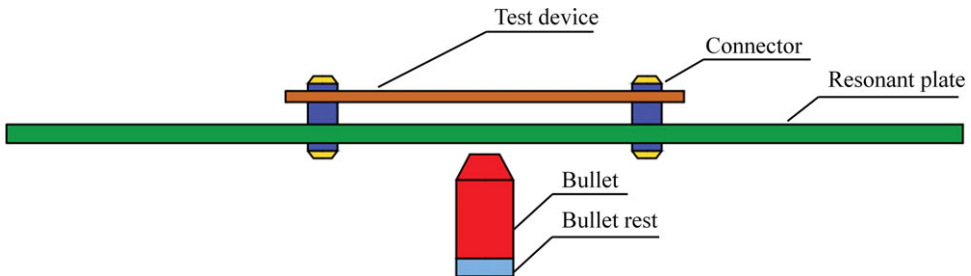***Figure 1.*** *Air cannon device.*

Figure 2. *Schematic diagram of the simulation device.*

the high-pressure thrust of the air chamber. According to the conservation of energy, the relationship between the pressure of the air chamber and the bullet velocity is shown in Equation (1).

$$pV = \alpha \frac{1}{2} m_d v^2 \tag{1}$$

where p is the pressure of air chamber, MPa, V is the volume of barrel, m^3, $m_d = 1.28$ kg is the mass of bullet, v is the velocity of bullet, m/s, and $\alpha = 0.5$ is the correction coefficient.

2.2 Theory of SRS

The SRS can realistically describe the pyroshock environment [19], ensuring the detection of precision instruments is more precise and secure. The SRS can be regarded as synthesising the maximum response of a series of Single Degree of Freedom (SDOF) systems with the same damping to a given transient time-domain signal [20]. As shown in Fig. 3, it is composed of the slope of low frequency, break frequency and the amplitude of high frequency, which has a tolerance range of ± 3 dB in practical applications [21].

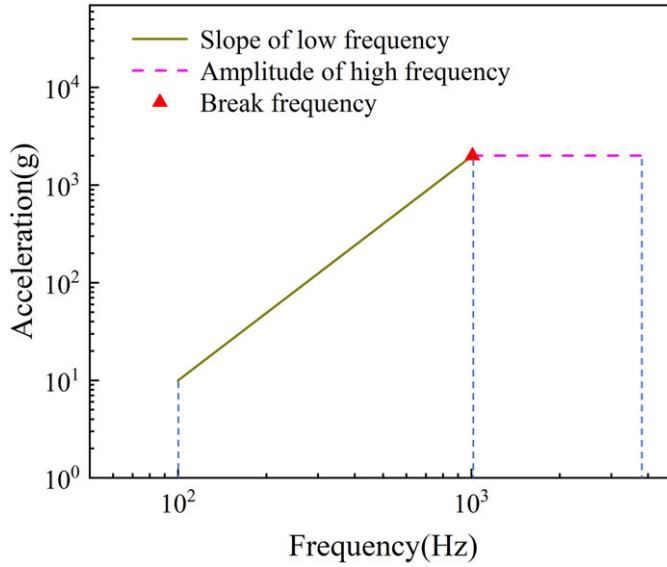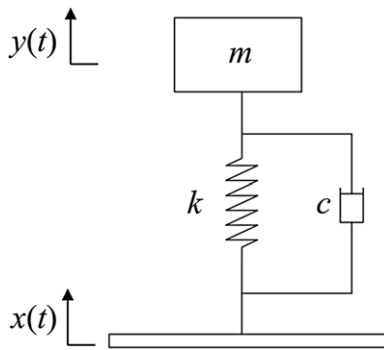**Figure 3.** *Standard SRS.*

Figure 4. *The mass-spring-damper system.*

The SDOF mass-spring-damper system of the shock test device is illustrated in Fig. 4. The equation of motion of the model is shown in Equation (2).

$$\begin{cases} m\ddot{y}(t) + c\dot{y}(t) + ky(t) = kx(t) + c\dot{x}(t) \\ \ddot{y}(t) + 2\xi\omega_n\dot{y}(t) + \omega_n^2 y(t) = \omega_n^2 x(t) + 2\xi\omega_n\dot{x}(t) \end{cases} \tag{2}$$

where $y(t)$ is the response of the system, $x(t)$ is the external input excitation, m is the mass of system, k is the stiffness of system, c is the damping of system, $\omega_n = \sqrt{k/m} = 2\pi f_n$ is the natural circular frequency, f_n is the natural frequency, $\omega_d = \omega_n\sqrt{1-\xi^2}$ is the damped natural circular frequency, $\xi = c \big/ (2\sqrt{km})$ is the damping coefficient.

When the resonant plate's initial displacement and initial velocity are zero, the solution of the above equation is presented in Equation (3).

$$\ddot{y}(t) = \frac{1}{\omega_d} \int_0^t \ddot{x}(\tau) e^{-\xi\omega_n(t-\tau)} \left[(\omega_d^2 - \xi^2\omega_n^2) \sin\omega_d(t-\tau) + 2\xi\omega_n\omega_d \cos\omega_d(t-\tau) \right] d\tau \tag{3}$$

Obviously, the absolute acceleration of the system is a function of natural frequency and damping coefficient. The maximum absolute acceleration variation curve corresponding to the natural frequency
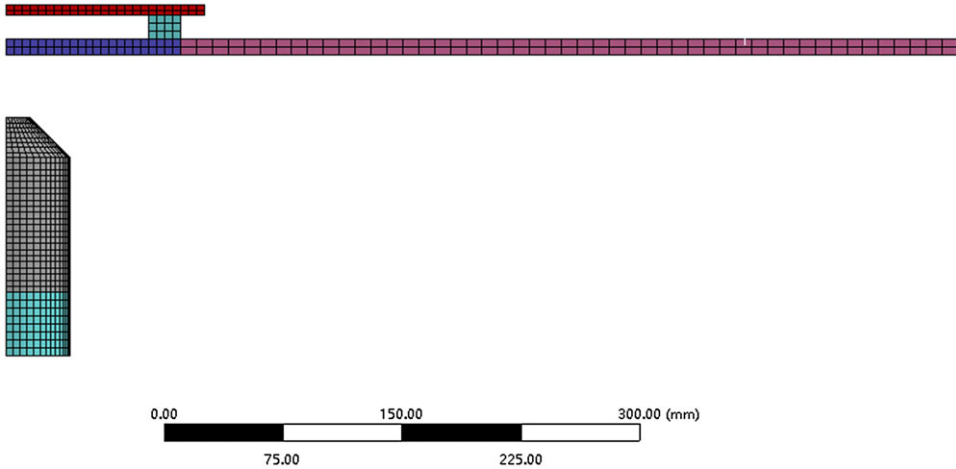
Figure 5. *Finite element model.*

can be obtained when the damping coefficient is constant, which is the acceleration shock response spectrum (ASRS). The ASRS required for the test can be obtained by adjusting the system's parameters, such as air chamber pressure, bullet length and material and the thickness and material of resonant plate. The following section will discuss the effects of the above parameters on the pyroshock environment.

2.3 Finite element model

Simulating the pyroshock environment using the bullet to impact the resonant plate is a typical transient dynamic problem. The ANSYS/LS-DYNA mainly adopts the Lagrange algorithm, so it has a powerful display dynamic analysis function, and thus, it is used for the numerical simulation study.

The finite element model is established according to the size of the device. Considering the symmetry between the model and the boundary, only a quarter of the model is established for computational efficiency. As exhibited in Fig. 5, the model has a total of 53,701 3D solid164 hexahedral elements, including 3,509 grids of bullet and 50,192 grids of the resonant plate. There is a gap between the bullet and the resonance plate to avoid initial contact. Furthermore, the resonant plate does not have initial displacement, stress and strain by imposing a fixed constraint. The bullet vertically impacts the resonant plate at different speeds, and the process is solved in the LS-DYNA solver module.

The SRSs after model mesh refinement are illustrated in Fig. 6. Among them, the break frequency of the three curves is 1425Hz, and the maximum relative error of the amplitude is 5.62%. The calculation results show that the variation of the three curves is small. Further refinement of the mesh can effectively improve the reliability of the model calculation results. Still, it also inevitably leads to huge consumption of computing time and space. It can be seen from the above calculations that the refinement of the number of grids has little effect on the results, so it can be considered that the model achieves grid independence.

2.4 Effect of adjustable parameters

2.4.1 Effect of pressure

The SRSs of different pressures are shown in Fig. 7. It can be found that these SRSs have similar line shapes, and the slope and the break frequency of the SRS are unchanged. This indicates that pressure is a crucial influential factor in the amplitude of the SRS. However, it has not obvious effect on the break frequency and the slope of the SRS. In addition, the amplitude of the SRS is increasing while the pressure is increasing.
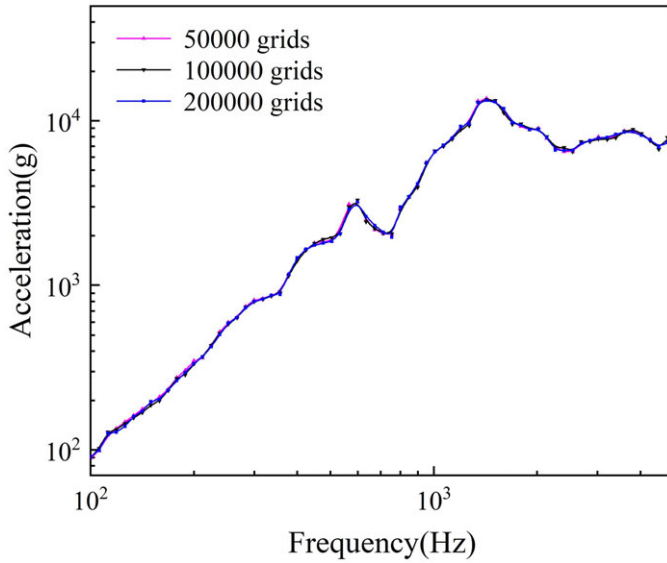
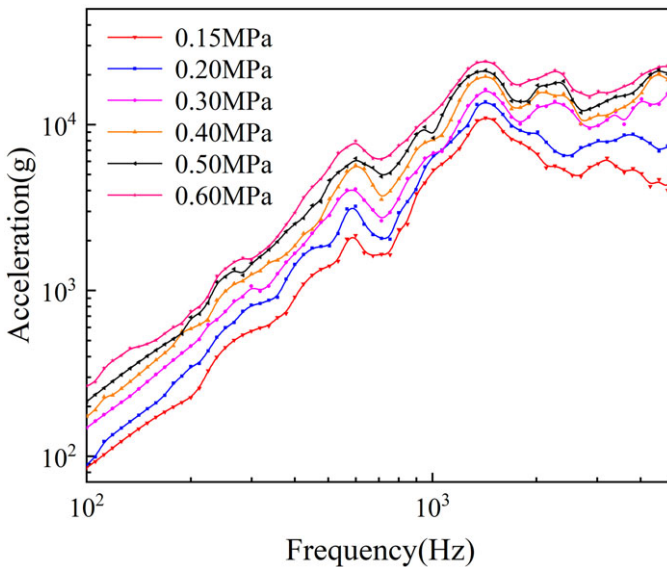***Figure 6.*** *SRSs of different grid numbers.*

Figure 7. *SRSs of different pressures.*

In order to research the quantitative relationship between the break frequency amplitude and the pressure, the bullet velocity is taken as the abscissa, and the break frequency amplitude is taken as the ordinate. And then, the least squares method was used to fit the relation curve, which is illustrated in Fig. 8. The relationship is expressed in Equation (4).

$$G = 692.5v \tag{4}$$

where G is the amplitude of break frequency of SRS, g, v is the bullet velocity, m/s.

By combining Equation (1) and Equation (4), the relationship between the break frequency amplitude and the pressure can be obtained as shown in Equation (5).
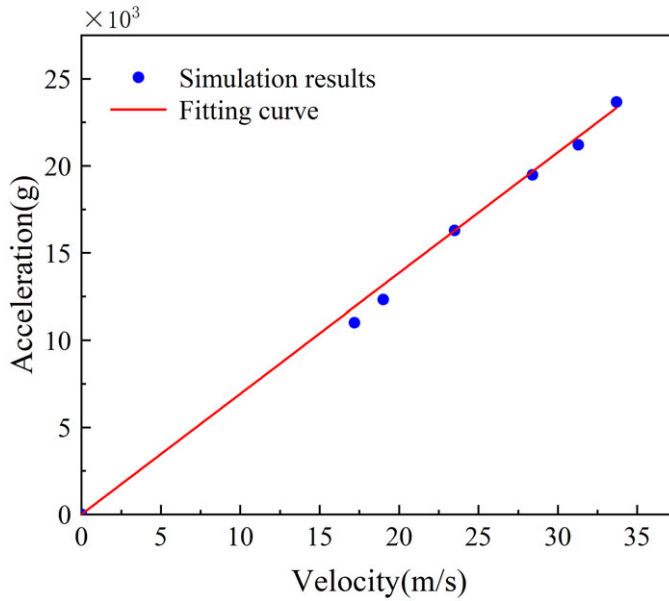
$$G = 83.8\sqrt{p} \tag{5}$$

Figure 8. *Fitting relationship curve of break frequency amplitudes and bullet velocity.*
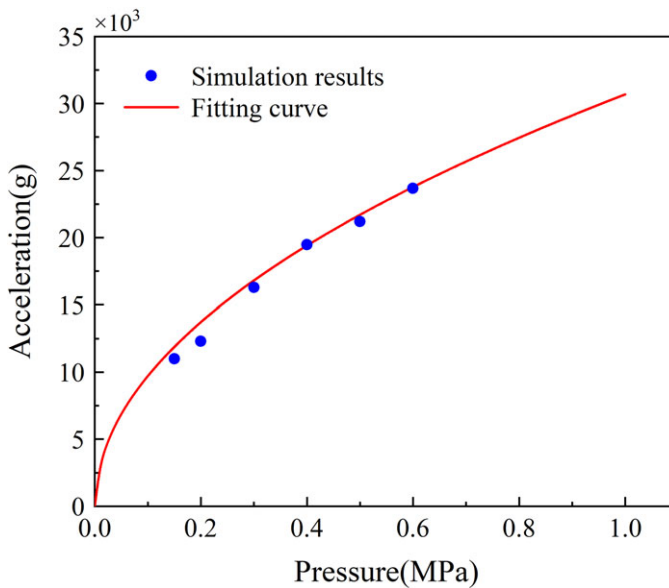

Figure 9. *Fitting relationship curve of break frequency amplitudes and pressure.*

The relationship between the break frequency amplitude and the pressure is illustrated in Fig. 9. The maximum error between the simulation result and the fitting curve is 2.71%, which is within the tolerance range of ±3 dB. Therefore, Equation (5) can well predict the break frequency amplitude of the SRS.

2.4.2 Effect of bullet length
The SRSs of the bullets with lengths of 80 mm, 130 mm and 150 mm are presented in Fig. 10. The amplitude fluctuation of the three curves is small, and their average error is 0.35 dB. The results show that the

Table 2. *Material parameters of bullet*

Material	Aluminium	Steel	Epoxy resin	Chrome alloy
Density (kg/m^3)	2,770	7,850	1,200	7,300
Elastic Modulus (MPa)	7.1×10^4	2×10^5	3.78×10^3	2×10^5
Poisson's ratio	0.33	0.3	0.35	0.3
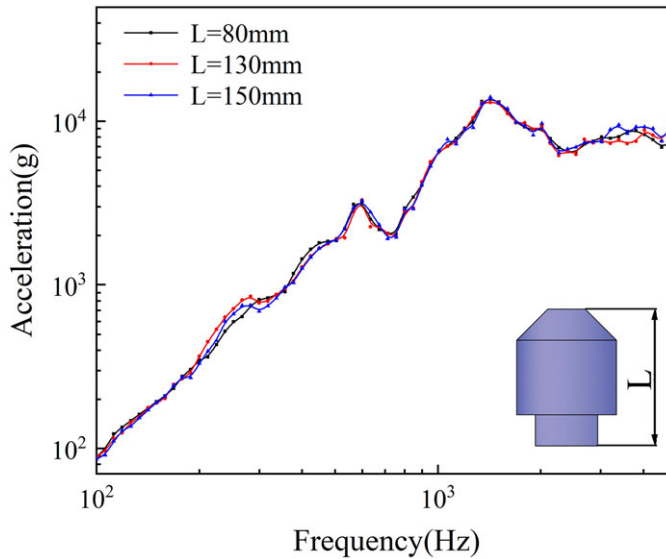
Figure 10. *SRSs of different bullet lengths.*

bullet length has little effect on the SRS of the resonant plate. Although the length of the bullet changed, its total kinetic energy did not change under the same working pressure. Since the energy transfer efficiency of the three bullets is the same when they impact the resonant plate, the energy transmitted to the resonant plate is unchanged. Therefore, it can be considered that the bullet length has a less significant effect on the pyroshock environment of the resonant plate.

2.4.3 Effect of bullet material

The SRSs of the bullets with three different materials are shown in Fig. 11, and the material parameters are listed in Table 2. There is a small bump at the frequency of 600 Hz, which should be the natural frequency of a certain order of the resonant plate. The vibration shape of this order is suppressed during the impact, and the dangerous frequency is still 1,425 Hz. Besides, the high-frequency amplitude of the SRS caused by the epoxy resin bullet is the largest, and the steel bullet is the smallest. The pyroshock environment simulated by the bullet of epoxy resin is more severe. This phenomenon shows that the bullet's material mainly affects the SRS's high-frequency amplitude and slope but not the break frequency.

In order to explore the internal reasons for the influence of bullet materials on SRS, the energy change curve of the bullet during the impact process is extracted as shown in Fig. 12. It can be found that the three bullets have the same initial kinetic energy, and the kinetic energy decreases rapidly during the impact process. Moreover, the energy attenuation time of the epoxy resin bullet is the shortest, and the attenuation time of the steel bullet is the longest. This phenomenon explains that the energy transfer efficiency of epoxy resin bullet is the highest in the impact process, resulting in more severe and worse environmental impacts.

The SRSs of bullets with different densities are presented in Fig. 13.The result shows that the high-frequency amplitude of the SRS caused by the chrome alloy is larger than that of steel, which indicates
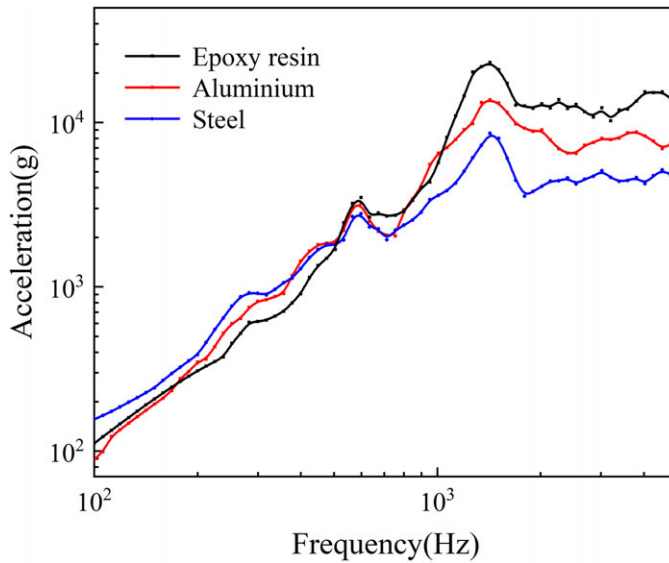
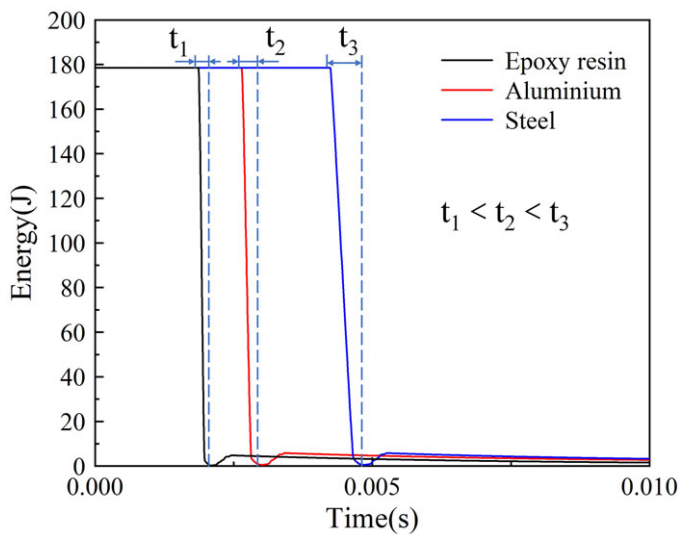**Figure 11.** *SRSs of different bullet materials.*

Figure 12. *Bullet energy change curves.*

that the density of bullet has an important influence on the high-frequency amplitude of the SRS. The density of the bullet will affect the energy transfer efficiency during the impact process, and ultimately affect the high-frequency amplitude of the SRS. In addition, the energy transfer efficiency of the bullet increases with the decrease of the density during the impact process, which eventually leads to the increase of the high-frequency amplitude.

2.4.4 Effect of thickness of resonant plate
The SRSs of the resonant plate with a thickness of 6–14 mm are shown in Fig. 14, and the parameters of the SRS are listed in Table 3. It can be found that the thickness of the resonant plate has a comprehensive effect on SRS. The break frequncy of the SRS is increasing while the resonant plate's thickness
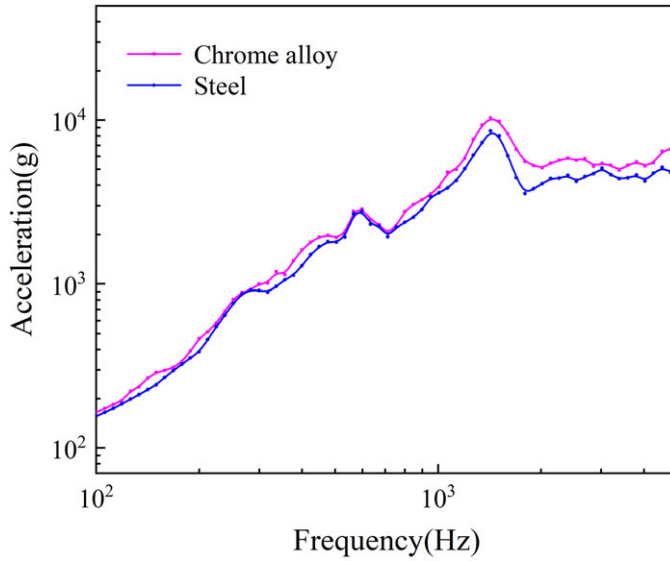
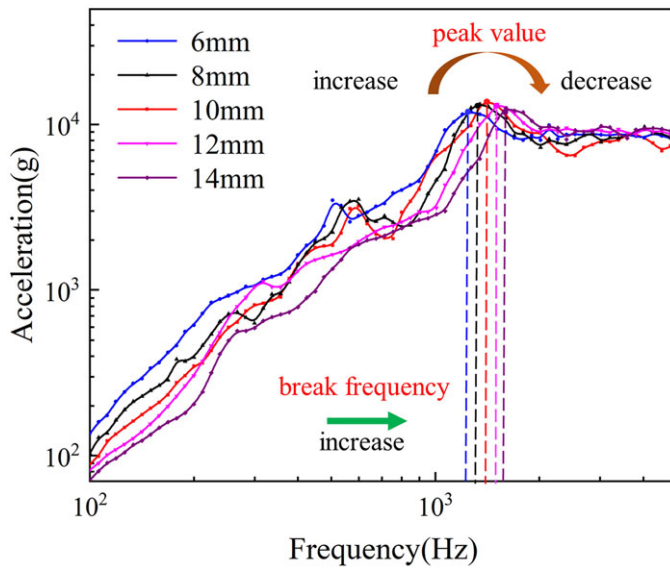**Figure 13.** *SRSs of different densities of bullets.*

Figure 14. *SRSs of different resonator plate thicknesses.*

is increasing. At the same time, the initial amplitude and the slope of low-frequency decrease gradually. The thickness of the resonant plate directly affects its natural frequency, and the initial amplitude decreases with the increase in the weight of the resonant plate. The break frequency amplitude has a trend of increasing first and then reducing. Moreover, the amplitude of break frequency is the largest when the thickness is 10 mm. Above results indicated that the resonant plate's thickness significantly effects the break frequency and the slope of the SRS, and the break frequency amplitude has a maximum value in a certain range.

Table 3. *SRS parameters of resonator plates with different thicknesses*

Thickness (mm)	Break frequency (Hz)	Amplitude of break frequency (g)	Slope of low-frequency (dB/oct)
6	1,270	12,642	9.84
8	1,345	13,235	9.76
10	1,425	13,713	9.56
12	1,500	13,181	8.73
14	1,610	12,534	7.74

Table 4. *Material parameters*

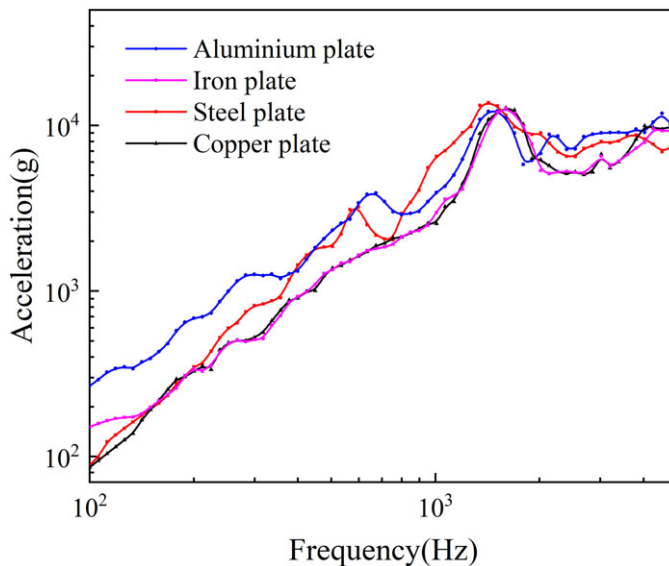| Material	Aluminium	Steel	Iron	Copper
Density (kg/m^3)	2,770	7,850	7,200	8,300
Elastic Modulus (MPa)	7.1×10^4	2×10^5	1.1×10^5	1.1×10^5
Poisson's ratio	0.33	0.3	0.28	0.34

Figure 15. *SRSs of resonator plate with different materials.*

2.4.5 Effect of material of resonant plate

The SRSs of the resonant plate with different materials are illustrated in Fig. 15, and the material parameters are shown in Table 4.

The figure shows that the slope of low frequency, break frequency and the amplitude of the SRS are different, indicating that the resonant plate material directly affects the SRS curve's shape. Also, it can be found that the curve of the iron plate and the copper plate are similar. This is because their same elastic modulus makes the system stiffness similar, ultimately leading to the resonant plate's similar dynamic response under impact. The initial amplitude of the SRS decreases with the increase of the density of the resonant plate, and the slope of low-frequency changes accordingly. The above analysis indicates that the resonant plate's elastic modulus plays an important role in the shape of the SRS, and the density affects the slope of low frequency.
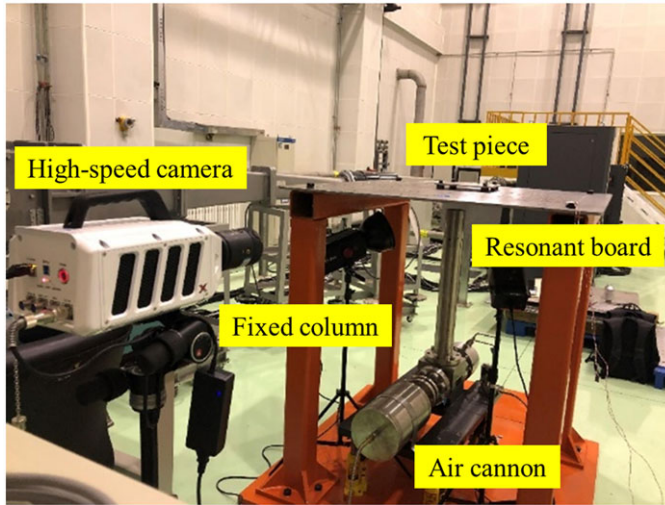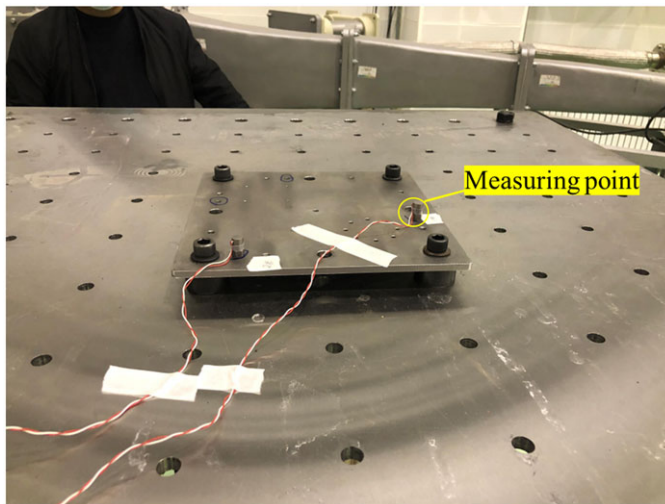
Figure 16. *Shock test device.*

Figure 17. *Accelerometer installation.*

3.0 Shock test

3.1 Shock test system

The implementation of the test rig which describe in section 2.1 is shown in Fig. 16. In order to be suitable for the fixation of various equipment sizes, a series of mounting holes are designed on the resonant plate. A high-speed camera is used to record the impact process of the bullet and calculate the bullet velocity. The installation position of the accelerometer is exhibited in Fig. 17, which is the same position as the measuring point in the numerical simulation study.

The air pressure was set to 0.15 MPa before the test began, and three repeated impact tests were carried out using the above setup. The acceleration histories of these three shock tests are shown in Fig. 18(a), and the SRSs are presented in Fig. 18(b). The acceleration response waveforms of the three tests are similar. Furthermore, the SRS curves are also consistent. The average error of SRSs is 0.22 dB, which is far less than the actual engineering requirements. Therefore, the device constructed has excellent repeatability and reliable test results.
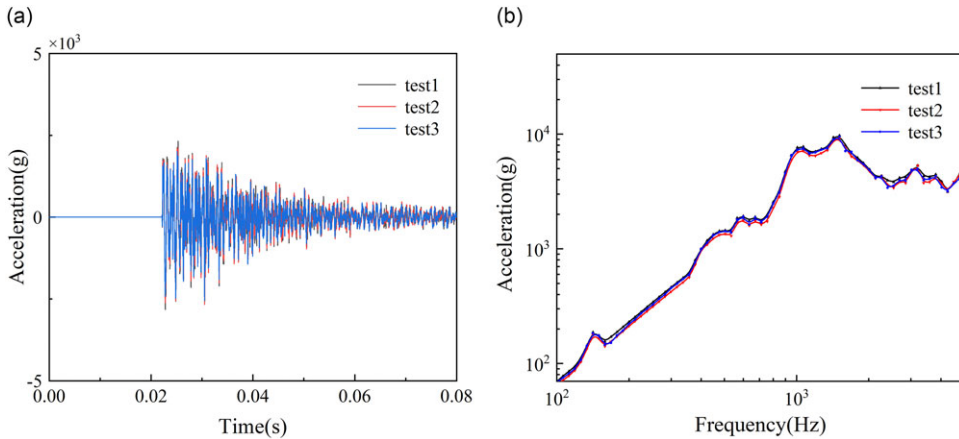
Figure 18. *Three curves of (a) acceleration histories and (b) shock response spectrum.*
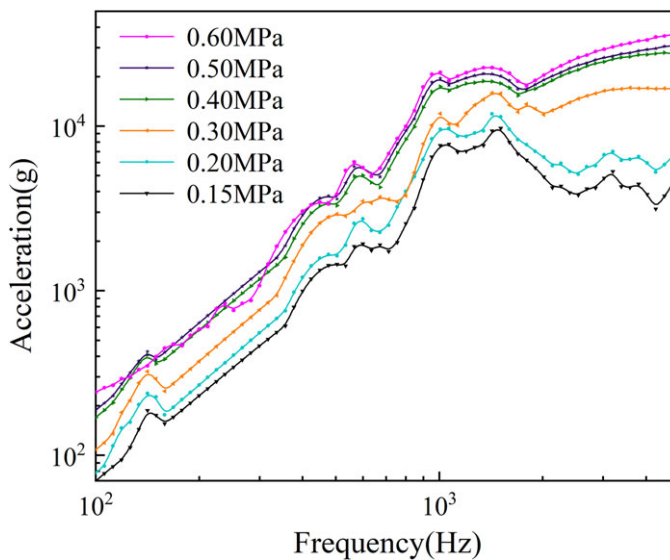

Figure 19. *SRSs of different pressures.*

3.2 Test results

3.2.1 Effect of pressure

The SRSs of different pressure conditions obtained from the test are shown in Fig. 19. The SRS amplitude increases with the pressure increase in the range of 0.15–0.60 MPa. However, the break frequency and the slope of the SRS did not change significantly. The comparison between the simulation results and the test results at a pressure of 0.15 MPa is illustrated in Fig. 20. It is obvious that the break frequency and the slope of the SRS are essentially consistent, and the simulation results are within the tolerance range of ±3 dB of the test results. The relationship between the break frequency amplitude and the bullet velocity obtained from the test and simulation is presented in Fig. 21(a). A linear relationship exists between the break frequency amplitude and the bullet velocity.

From Equation (3), the relationship between the break frequency amplitude and the pressure of the test device is shown in Fig. 21(b). The relationship is displayed as

$$G = 81.9\sqrt{p} \tag{6}$$

where G is the amplitude of break frequency, g, p is the pressure, MPa.
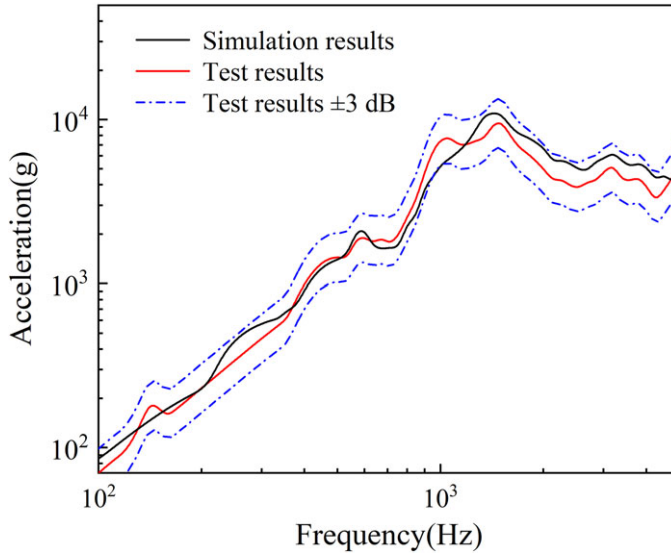
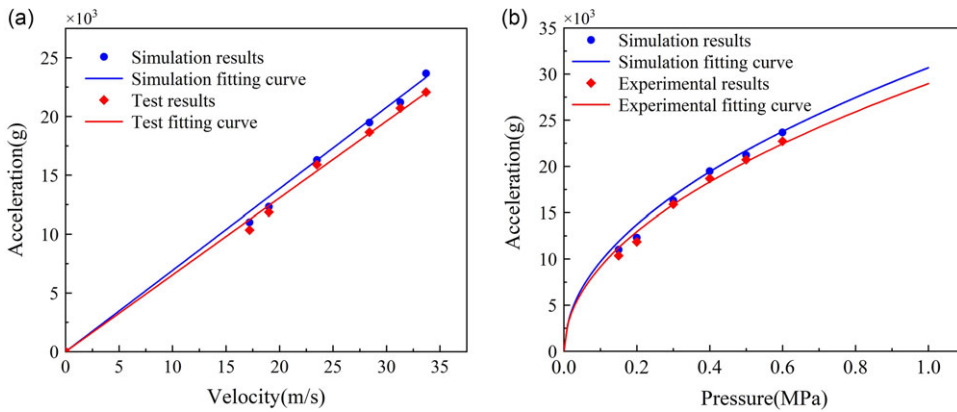***Figure 20.*** *Comparison of numerical and test results.*

Figure 21. *Fitting relationship curve of (a) break frequency amplitude and the bullet velocity and (b) break frequency amplitude and the pressure.*

The analysis above shows a square root function relationship between the break frequency amplitude and the pressure. Once given the break frequency amplitude of the SRS, the chamber pressure required by the test can be calculated by Equation (6). In addition, it can be found that there is a good consistency between the results of the simulation and the test. Therefore, the finite element model has good accuracy, and the simulation results are reliable.

3.2.2 Effect of bullet length

The SRSs of bullets with different lengths obtained from the test are shown in Fig. 22. It can be discovered that the curves of the three cases are similar, and the average error of the amplitude is 0.28 dB. This effect caused by bullet length is small, and the simulation results are consistent with the experimental results. The above analysis indicates that the bullet length has no significant effect on the simulation of the pyroshock shock environment.
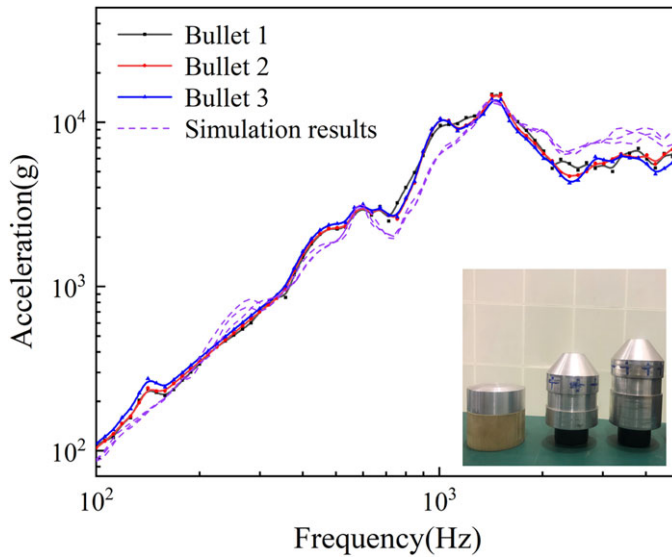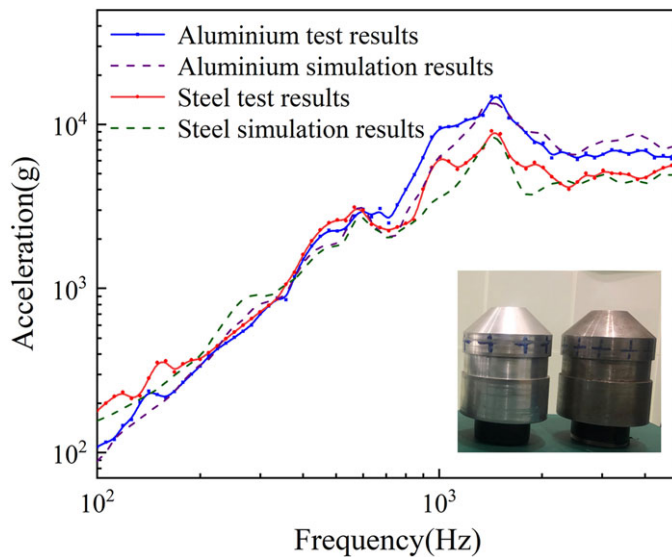
Figure 22. *SRSs of different length bullets.*

Figure 23. *SRSs of different material bullets.*

3.2.3 Effect of bullet material

The bullets made of 7A04 aluminium and 45 steel were selected for shock test, and the SRSs of the two bullets are illustrated in Fig. 23. It can be found that the material of the bullet has a significant effect on the high-frequency amplitude and the slope of the SRS. In addition, the reliability of the simulation results is verified by comparing the simulation results with the experimental results. Because the density of the aluminium bullet is smaller, it has higher energy transfer efficiency. As a result, the high-frequency amplitude of the SRS caused by the aluminium bullet is larger. The above analysis shows that the bullet's material significantly affects the high-frequency amplitude of the SRS, and the high-frequency amplitude decreases with the increase of the bullet density.

4.0 Conclusions

This paper designed a pyroshock environment simulation device with adjustable parameters. And proposed the numerical model of the resonant plate, the structure response is solved by the explicit dynamic software ANSYS/LS-DYNA. Combined with the theory of SRS, the effect rules of adjustable parameters on SRS are studied systematically. The experiments were carried out to validate the finite element model. Some conclusions are as follows:

(1) The pyroshock environment simulation device excited by air cannon can simulate a high-amplitude pyroshock environment well.

(2) The air cannon's pressure mainly affects the SRS's amplitude. The amplitude of SRS increases with the increase of pressure in the range of 0.15–0.60 MPa, the break frequency amplitude has a square root function relationship with the pressure.

(3) The high-frequency amplitude of the SRS is affected by the energy transfer efficiency of the bullet and decreases while bullet density increases.

(4) The SRS break frequency increases with the resonant plate's thickness. The elastic modulus of the resonant plate affects the line shape of the SRS, and affects the slope of low frequency in conjunction with density.

References

[1] Huang, H.J., Wang, J.P., Mao, Y.J., Yue, X.H. and Lv, J. Influence of pretightening force of explosive bolts on impulse response, *J. Vib. Shock*, 2015, **34**, (16), pp 166–169.

[2] Ding, J.F., Zhao, X. and Han, Z.Y. Research development of spacecraft pyroshock technique, *J. Astronaut.*, 2014, **35**, (12), pp 1339–1349.

[3] Zhao, H.D., Liu, W., Ding, J.F., Sun, Y., Li, X. and Li, Y. Numerical study on separation shock characteristics of pyrotechnic separation nuts, *Acta Astronaut.*, 2018, **151**, pp 893–903.

[4] Lee, J.R., Chen, C.C. and Kong, C.W. Review of pyroshock wave measurement and simulation for space systems, *Measurement*, 2012, **45**, (4), pp 631–642.

[5] Mao, Y.J. and Li, Y.L. Advances in simulation techniques of pyroshock environments, *Missile Space Veh.*, 2007, (4), pp 37–44.

[6] Smirnov, N.N., Betelin, V.B., Nikitin, V.F., Stamov, L.I. and Altoukhov, D.I. Accumulation of errors in numerical simulations of chemically reacting gas dynamics, *Acta Astronaut.*, 2015, **117**, pp 338–355.

[7] Zhao, H.D., Hao, Z.W., Liu, W., Ding, J.F., Sun, Y., Zhang, Q.H. and Liu, Y.Z. The shock environment prediction of satellite in the process of satellite-rocket separation, *Acta Astronaut.*, 2019, **159**, pp 112–122.

[8] Monti, R. and Gasbarri, P. Dynamic load synthesis for shock numerical simulation in space structure design, *Acta Astronaut.*, 2017, **137**, pp 222–231.

[9] Mao, B.Y., Xie, S.L., Xu, M.L., Zhang, X.N. and Zhang, G.H. Simulated and experimental studies on identification of impact load with the transient statistical energy analysis method, *Mech. Syst. Signal Process.*, 2014, **46**, (2), pp 307–324.

[10] Ma, B.J., Zhang, J.H. and Wu, J. Applications and effects of pyrotechnic explode loading in shock environment simulation experiment of rocket separation, *Struct. Environ. Eng.*, 2007, **35**, (5), pp 1–7.

[11] Zhao, H.D., Ding, J.F., Liu, W., Hao, Z.W., Sun, Y., Zhang, Q.H. and Liu, Y.Z. Simulator of pyroshock environment and effect rules of its adjustable parameters, *Chinese J. Aeronaut.*, 2020, **33**, (2), pp 609–620.

[12] Velmurugan, R. and Najeeb, E.M. Study of far-field pyroshock responses of composite panels, *J. Vib. Acoust.*, 2014, **136**, (3), pp 1–10.

[13] Zhao, H.D., Sun, Y., Ding, J.F., Hao, Z.W., Liu, W., Wang, X. and Liu, Y.Z. Simulation techniques of pyroshock environment under the excitation of a light gas gun, *J. Vib. Shock*, 2021, **40**, (22), pp 1–10.

[14] Jang, J.K. and Lee, J.R. Non-destructive visualisation of linear explosive-induced Pyroshock using phase arrayed laser-induced shock in a space launcher composite, *J. Phys. Conf.*, 2015, **628**, p 012104.

[15] Lee, J.R., Jang, J.K., Choi, M. and Kong, C.W. Visualisation and simulation of a linear explosive-induced pyroshock wave using Q-switched laser and phased array transducers in a space launcher composite structure, *Opt. Laser Technol.*, 2015, **67**, pp 12–19.

[16] Wang, X.X., Qin, Z.Y., Ding, J.F., Zhang, Z.Y. and Chu, F.L. Analysis of shock response induced by laser and its features, *J. Astronaut.*, 2018, **39**, (4), pp 464–470.

[17] Yan, H.P., Qin, Z.Y., Chu, F.L., Zhang, W. and Wang, X. Dynamic response of aluminum honeycomb panels to high-frequency laser shock excitations, *J. Spacecr. Rockets*, 2020, **57**, (1), pp 198–201.

[18] Mulville, D.R. Pyroshock test criteria: NASA STD-7003A. Washington, D.C.: NASA, 1999.

[19] Alexander, J.E. Shock response spectrum-a prime, *J. Sound Vib.*, 2009, **43**, (6), pp 6–14.

[20] Wang, X.X., Qin, Z.Y., Ding, J.F. and Chu, F.L. Finite element modeling and pyroshock response analysis of separation nuts, *Aerosp. Sci. Technol.*, 2017, **68**, pp 380–390.

[21] Botta, F. and Cerri, G. Shock response spectrum in plates under impulse loads, *J. Sound Vib.*, 2007, **308**, (3–5), pp 563–578.